# Pulse Shaping Techniques for Testing Brittle Materials with a Split Hopkinson Pressure Bar

## by D. J. Frew, M. J. Forrestal, and W. Chen

ABSTRACT—We present pulse shaping techniques to obtain compressive stress–strain data for brittle materials with the split Hopkinson pressure bar apparatus. The conventional split Hopkinson pressure bar apparatus is modified by shaping the incident pulse such that the samples are in dynamic stress equilibrium and have nearly constant strain rate over most of the test duration. A thin disk of annealed or hard C11000 copper is placed on the impact surface of the incident bar in order to shape the incident pulse. After impact by the striker bar, the copper disk deforms plastically and spreads the pulse in the incident bar. We present an analytical model and data that show a wide variety of incident strain pulses can be produced by varying the geometry of the copper disks and the length and striking velocity of the striker bar. Model predictions are in good agreement with measurements. In addition, we present data for a machineable glass ceramic material, Macor, that shows pulse shaping is required to obtain dynamic stress equilibrium and a nearly constant strain rate over most of the test duration.

KEY WORDS—Hopkinson bar, pulse shaping, brittle materials, high strain rate

## Introduction

The split Hopkinson pressure bar (SHPB) or Kolsky bar technique, originally developed by Kolsky,[1,2] has been used by many investigators to obtain dynamic compression properties of solid materials. The evolution of this experimental method and recent advances are discussed by Nicholas,[3] Ellwood et al.,[4] Franz et al.,[5] Follansbee,[6] Nemat-Nasser et al.,[7] Ramesh and Narasimhan,[8] Gray,[9] and Gray and Blumenthal.[10] This technique has mostly been used to study the plastic flow stress of metals that undergo large strains at strain rates between $10^2$–$10^4$ s$^{-1}$. As discussed by Yadav et al.,[11] data for the compressive flow stress of metals are typically obtained for strains larger than a few percent because the technique is not capable of measuring the elastic and early yield behavior. By contrast, most of the material behavior of interest for relatively brittle materials such as ceramics[12,13] and rocks[14] occurs at strains less than about 1.0 percent.

D. J. Frew is a Senior Member of Technical Staff, Sandia National Laboratories, Albuquerque, NM 87185-1174. M. J. Forrestal (SEM Member) is a Distinguished Member of Technical Staff, Sandia National Laboratories, Albuquerque, NM 87185-1174. W. Chen (SEM Member) is an Associate Professor, Department of Aerospace and Mechanical Engineering, The University of Arizona, Tucson, AZ 85721-0119.

Some of the advantages and necessities for shaping the incident pulse for split Hopkinson pressure bar (SHPB) experiments were discussed twenty years ago. Franz et al.[5] and Follansbee[6] wrote review papers that discussed pulse shaping for SHPB experiments with metal samples. In these review papers, the authors emphasized that a slowly rising incident pulse is preferred to a pulse that rises steeply in order to minimize the effects of dispersion and allow the sample to achieve dynamic stress equilibrium. Franz et al.[5] and Follansbee[6] discuss experimental techniques for pulse shaping and a numerical procedure[15] for correcting raw data for wave dispersion in the bars. To shape the incident pulse these authors[5,6] machined a large radius on the impact face of the striker bar or placed a tip material between the striker and incident bars. The tip material or pulse shaper was a disk slightly larger than the bars and 0.1–2.0 mm thick. The pulse shaper materials were paper, aluminum, brass or stainless steel. Franz et al.[5] present experimental results that show the advantages of pulse shaping for a 3041 stainless steel sample at an approximate strain rate of 4500 s$^{-1}$. In addition, these authors[5] and Ellwood et al.[4] show that a properly chosen tip material or pulse shaper can also be used to generate a nearly constant strain rate in the sample. Gray[9] and Gray and Blumenthal[10] present additional information in recent survey papers that include these subjects. However, Duffy et al.[16] were probably the first authors to use pulse shapers to smooth pulses generated by explosive loading for the torsional Hopkinson pressure bar.

While pulse shaping techniques have been successfully used to achieve the goals of many different experiments, pulse shapers are usually designed by experimental trials that exclude a model to guide the design parameters. For other examples, Wu and Gorham[17] used paper on the impact surface of the incident bar to eliminate high frequency oscillations in the incident pulse for Kolsky compression bar experiments. Togami et al.[18] used a thin, Plexiglas disk to produce nondispersive compression pulses in an incident bar, and Chen et al.[19] used a polymer disk to spread the incident compressive pulses for experiments with elastomers. Christensen et al.[20] used striker bars with a truncated-cone on the impact end in an attempt to produce ramp pulses. In contrast to other pulse shaping studies, Nemat-Nasser et al.[7] model the plastic deformation of an OFHC copper pulse shaper, predict the incident strain pulse, and show good agreement with some measured incident strain pulses.

In an ideal Kolsky compression bar experiment, the sample should be in dynamic stress equilibrium and deform at a nearly constant strain rate over most of the test duration. For

the stress–strain response of relatively brittle materials that have a nearly linear response to failure and failure strains less than about 1.0 percent, Nemat-Nasser et al.[7] recommended pulse shaping with an OFHC copper disk to achieve a ramp pulse in the incident bar. Again, these authors[7] also have an experimentally verified model for pulse shaping with an OFHC copper disk to predict the incident pulses. In addition, Ravichandran and Subhash[21] present a method of characteristics analysis for wave motions in a ceramic sample and provide a criterion for dynamic sample equilibrium. More recently, Frew et al.[14] extended this work[7,21] to obtain high-rate, stress–strain data for limestone samples. Data from experiments with limestone samples and analytical models showed that the samples were in dynamic stress equilibrium and had nearly constant strain rates over most the test durations for a ramp pulse in the incident bar. This paper[14] also presents data that showed the ramp pulse durations could be controlled such that samples could be unloaded just prior to failure.

In this study, we build on the referenced work and present some new analytical models and experimental data for testing brittle materials with the Kolsky pressure bar technique. In the next section, we review the SHPB technique and discuss our apparatus. Then we present analytical models that predict the evolutionary process for sample equilibrium and constant strain rate. In the following section, we focus on the details of pulse shaping with both annealed and hard C11000 copper[22] disks. Experiments with both OFHC and C11000 copper pulse shapers showed that the C11000 materials could be driven to larger strains without breakup or fracture and remain more circular after deformation. Thus, the pulse shaper material response model presented by Nemat-Nasser et al.[7] was generalized to accurately predict the large strain responses of the C11000 copper[22] pulse shapers. Finally, we present stress–strain data for a machinable glass ceramic, Macor,[23] that shows pulse shaping is required to obtain dynamic stress equilibrium and a nearly constant strain rate over most of the test duration.

## Split Hopkinson Pressure Bar (SHPB) or Kolsky Bar

As shown in Fig. 1, a conventional split Hopkinson pressure bar (SHPB) consists of a striker bar, an incident bar, a transmission bar, and a sample placed between the incident and transmission bars. A gas gun launches the striker bar at the incident bar and that impact causes an elastic compression wave to travel in the incident bar towards the sample. When the impedance of the sample is less than that of the bars, an elastic tensile wave is reflected into the incident bar and an elastic compression wave is transmitted into the transmission bar. If the elastic stress pulses in the bars are nondispersive and the specimen deforms with homogeneous deformation, the elementary theory for wave propagation in bars can be used to calculate the sample response from measurements taken with strain gages mounted on the incident and transmission bars. Strain gages mounted on the incident bar measure the incident $\varepsilon_i$ and reflected $\varepsilon_r$ strain pulses, and strain gages mounted on the transmission bar measure the transmitted $\varepsilon_t$ strain pulse. Nicholas[3] and Gray[9] present equations that describe the sample response in terms of the measured strain signals.

For this study the incident and transmission bars were made from the same material with equal cross-sectional areas.

As shown in Fig. 1, the bars have density $\rho$, Young's modulus $E$, bar wave speed $c$, and cross-sectional area $A$. Since we only focus on brittle materials that have failure strains less than about 1.0 percent, we need only use engineering stress, strain, and strain–rate measures. In addition, we take stress positive in compression, strain positive in contraction, and particle velocity positive to the right in Fig. 1. Figure 1 also shows the sample has cross-sectional area $A_s$ and length $l_0$. We take subscripts 1 and 2 to represent the locations of the ends of the sample.

From Nicholas[3] or Gray[9]

$$\sigma_1 = \frac{EA}{A_s}(\varepsilon_i + \varepsilon_r) \tag{1a}$$

$$\sigma_2 = \frac{EA}{A_s}\varepsilon_t. \tag{1b}$$

If $\sigma_1 = \sigma_2$, the stresses on both ends of the sample are equal, the sample is in dynamic stress equilibrium, and the stress, strain rate, and strain are given by

$$\sigma_s = \frac{EA}{A_s}\varepsilon_t \tag{2}$$

$$\frac{d\varepsilon_s}{dt} = \frac{-2c}{l_0}\varepsilon_r \tag{3}$$

$$\varepsilon_s = \frac{-2c}{l_0}\int_0^t \varepsilon_r(\tau)d\tau. \tag{4}$$

As discussed in detail by Ravichandran and Subhash,[21] Gray,[9] Gray and Blumenthal,[10] and Frew et al.,[14] Eqs (2), (3), and (4) assume that the sample is in dynamic stress equilibrium. Equilibrium should first be examined by comparing the stresses $\sigma_1$ and $\sigma_2$ at the ends of the sample given by Eqs (1a) and (1b). If $\sigma_1$ and $\sigma_2$ are in reasonable agreement, only then it is reasonable to use Eqs (2), (3), and (4) to calculate sample stress, strain rate, and strain.

The striker, incident, and transmission bars shown in Fig. 1 were made from high strength, maraging VM 350 steel (Vasco Pacific, Montebello, CA) and have density $\rho = 8100$ kg/m$^3$, Young's modulus $E = 200$ GPa, and bar wave velocity $c = 4970$ m/s. The incident and transmission bars had lengths of 2130 and 1370 mm, respectively, and the strain gages shown in Fig. 1 were located at 1065 mm from the impact surface of the incident bar and at 685 mm from the sample/ bar interface on the transmission bar. We used both 12.7 and 19.0 mm diameter bars. The lengths of the striker bars were varied to obtain the desired incident bar pulse shapes.

The striker bar is launched by a gas gun that has a bore diameter larger than the striker bar diameter, so the striker bar is fitted with three nylon bore-riders (sabots). The bore-riders are nylon cylinders that make a snug fit for the striker bar in the gun bore. For good alignment, the sabot package is designed so that two bore-riders are in the gun bore at the time of impact. We learned early in this study that the added mass of the bore-riders needed to be included in the striker bar wave analysis for predicting incident strain pulses. Forrestal et al.[24] present a derivation of the elementary theory for the striker bar by using an effective density $\rho_{st}$, where $\rho_{st}$ is the total mass of the striker bar and bore-riders divided by the volume of the striker bar. The wave velocity for the striker
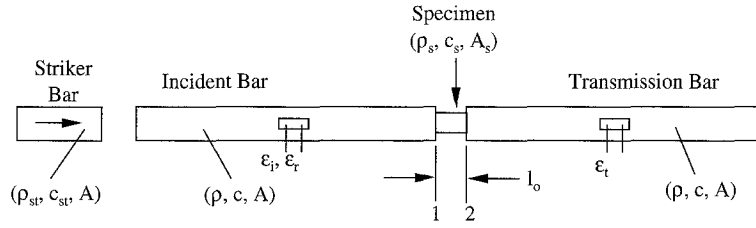
Fig. 1—Schematic of a conventional split Hopkinson pressure bar (SHPB) or Kolsky bar

bar is taken as $c_{st}^2 = E/\rho_{st}$, where $E$ is Young's modulus for the striker bar.

## Models for Sample Equilibrium and Constant Strain Rate

In a recent paper,[14] we presented models that predict the evolutionary process for sample equilibrium and constant strain rate for brittle materials that have a linear stress–strain response until failure. These models were limited to a ramp stress pulse in the incident bar, but provided experimental design information for testing limestone samples. In our more recent work with brittle materials, we learned that it was relatively easy to obtain sample equilibrium and more difficult to obtain a nearly constant strain rate over most of the test duration. To assist our experimental design procedures prior to testing, we extend our previous models[14] to include a general incident stress pulse. The more general models allow us to examine incident pulses that produce nearly constant strain rates in the sample for a broader range of strain rates. The first model assumes that the sample is in dynamic stress equilibrium and predicts strain and strain rate versus time. For the second model, we perform a wave propagation analysis on the interaction of the sample with the incident and transmission bars. This second model predicts the stress–time histories on either side of the sample.

From the derivations in Frew et al.,[14] sample strain is governed by the differential equation

$$\frac{d\varepsilon_s}{dt} + \frac{2A_s E_s}{\rho c A l_0}\varepsilon_s = \frac{2\sigma_i(t)}{\rho c l_0} \qquad (5)$$

where the sample has the linear stress–strain relation

$$\sigma_s = E_s \varepsilon_s. \qquad (6)$$

In Eq (5), $\sigma_i(t)$ is the incident pulse and $t = 0$ when the incident pulse reaches the incident bar/sample interface. For a polynomial incident stress

$$\sigma_i(t) = \sigma_0 + Mt + Nt^2 \qquad (7)$$

Eq (5) has solutions

$$\frac{d\varepsilon_s}{dt} = \frac{2\sigma_0\gamma}{E_s r t_0}\exp\left(\frac{-2t}{r t_0}\right) + \frac{\gamma M}{E_s}\left[1 - \exp\left(\frac{-2t}{r t_0}\right)\right]$$

$$+ \frac{N\gamma t_0 r}{E_s}\left[-1 + \frac{2t}{r t_0} + \exp\left(\frac{-2t}{r t_0}\right)\right] \qquad (8a)$$

$$\varepsilon_s = \frac{\sigma_0\gamma}{E_s}\left[1 - \exp\left(\frac{-2t}{r t_0}\right)\right]$$

$$+ \frac{\gamma M}{E_s}\left[t - \frac{r t_0}{2}\left(1 - \exp\left(\frac{-2t}{r t_0}\right)\right)\right]$$

$$+ \frac{N\gamma(r t_0)^2}{2E_s}\left[1 + \left(\frac{-2t}{r t_0}\right) + 2\left(\frac{t}{r t_0}\right)^2 - \exp\left(\frac{-2t}{r t_0}\right)\right] \qquad (8b)$$

$$\gamma = \frac{A}{A_s}, \quad r = \frac{A\rho c}{A_s \rho_s c_s}, \quad t_0 = \frac{l_0}{c_s}. \qquad (8c)$$

Equations (8a) and (8b) give closed-form solutions for the strain rate and strain in the sample. However, this model assumes that the sample is in equilibrium.

For the second model, we perform a wave propagation analysis on the interaction of the sample with the incident and transmission bars. Following the procedure developed by Frew et al.,[14] the stress in the sample at interface 1 shown in Fig. 1 is

$$\sigma_1 = \frac{2\gamma}{r + 1}\sigma_i(t), \quad 0 \le t < 2t_0 \qquad (9a)$$

$$\sigma_1 = \frac{2\gamma}{r + 1}\sigma_i(t) + \frac{2\gamma}{r + 1}\left[\left(\frac{r - 1}{r + 1}\right) + \left(\frac{r - 1}{r + 1}\right)^2\right]$$

$$\sigma_i(t - 2t_0), \quad 2t_0 \le t < 4t_0 \qquad (9b)$$

$$\sigma_1 = \frac{2\gamma}{r + 1}\sigma_i(t) + \frac{2\gamma}{r + 1}\left[\left(\frac{r - 1}{r + 1}\right) + \left(\frac{r - 1}{r + 1}\right)^2\right]$$

$$\sigma_i(t - 2t_0) + \frac{2\gamma}{r + 1}\left[\left(\frac{r - 1}{r + 1}\right)^3 + \left(\frac{r - 1}{r + 1}\right)^4\right]$$

$$\sigma_i(t - 4t_0), \quad 4t_0 \le t < 6t_0 \qquad (9c)$$

and the stress at interface 2 is

$$\sigma_2 = 0, \quad 0 \le t < t_0 \qquad (10a)$$

$$\sigma_2 = \frac{2\gamma}{r + 1}\left[1 + \left(\frac{r - 1}{r + 1}\right)\right]\sigma_i(t - t_0)$$

$$t_0 \le t < 3t_0 \qquad (10b)$$

$$\sigma_2 = \frac{2\gamma}{r + 1}\left[1 + \left(\frac{r - 1}{r + 1}\right)\right]\sigma_i(t - t_0) + \frac{2\gamma}{r + 1}\left[\left(\frac{r - 1}{r + 1}\right)^2\right.$$

$$\left. + \left(\frac{r - 1}{r + 1}\right)^3\right]\sigma_i(t - 3t_0), \quad 3t_0 \le t < 5t_0. \qquad (10c)$$

The $n$th term for Eqs (9) and (10) is

$$\frac{2\gamma}{r+1}\left[\left(\frac{r-1}{r+1}\right)^{n-1} + \left(\frac{r-1}{r+1}\right)^{n}\right]\sigma_i(t - nt_0),$$

$$\text{for } nt_0 \le t < (n+2)t_0,$$

where $t_0$ is given by Eq (8c) and corresponds to one wave travel time through the sample. Therefore, $\sigma_1$ and $\sigma_2$ can easily be calculated for times greater than those given by Eqs (9) and (10).

## Pulse Shaping

As previously discussed, the conventional split Hopkinson pressure bar apparatus is modified by shaping the incident pulse such that the samples are in dynamic stress equilibrium and have nearly constant strain rate over most of the test duration. To achieve these ideal test conditions for brittle materials, we conducted experiments with both OFHC and C11000[22] copper pulse shapers and showed a superior performance by the C11000 materials. In particular, the C11000 pulse shapers could be driven to larger strains without breakup or fracture and remained more circular after deformation. Thus, the previous model[7] for OFHC copper was extended to accommodate the large strains obtained with the C11000 copper pulse shaper materials. In addition, we modified the equations that govern wave propagation in the striker bar to incorporate the added mass from the sabot[24] and included elastic, rather than rigid, unloading in the pulse shaping analysis. Incident pulse model predictions will be shown to be in good agreement with strain measurements.

Figure 2(a) shows a schematic of the impact end of the SHPB apparatus with a pulse shaper that is attached with a light coating of grease. In Fig. 2(a), $a_0$ and $h_0$ are the initial cross-sectional area and thickness of the pulse shaper. When the striker bar impacts the pulse shaper at velocity $V_0$, compressive forces are gradually transferred from the pulse shaper to the incident bar. The deformation of the pulse shaper increases its load carrying capacity by increasing its cross-sectional area and by strain hardening of the pulse shaping material. As will be shown later, the monotonic increase of the load carrying capacity of the pulse shaper causes longer duration pulses in the incident bar.

### Pulse Shaping Model

For an incompressible material and a homogeneous deformation, mass conservation gives

$$a_0 h_0 = a(t)h(t),\tag{11}$$

where $a(t)$ and $h(t)$ are the current cross-sectional area and thickness of the pulse shaper. The axial engineering strain in the pulse shaper is given by

$$\varepsilon_p(t) = \frac{h_0 - h(t)}{h_0} = 1 - \frac{h(t)}{h_0},\tag{12}$$

which is positive in contraction. From Eqs (11) and (12), the current cross-sectional area of the pulse shaper can be

written in terms of the original area and axial strain in the pulse shaper. Thus,

$$a(t) = \frac{a_0}{1 - \varepsilon_p(t)}.\tag{13}$$

The axial force exerted by the pulse shaper on the ends of the striker and incident bars is

$$T(t) = \sigma_p(t)a(t) = \sigma_i(t)A = \sigma_{st}(t)A,\tag{14}$$

where $\sigma_p(t)$ is the true axial stress in the pulse shaper, $\sigma_i(t)$ is from the compressive stress wave travelling to the right in the incident bar, and $\sigma_{st}(t)$ is from the compressive stress wave travelling to the left in the striker bar. From Eq (14), the bar stresses at the pulse shaper/ bar interfaces are

$$\sigma_i(t) = \sigma_{st}(t) = \frac{\sigma_p(t)a(t)}{A}.\tag{15}$$

For now, let $\sigma_p(t)$ be defined by the general form of a one-dimensional stress–strain relationship

$$\sigma_p = \sigma_0 g(\varepsilon_p),\tag{16}$$

where $\sigma_0$ is a constant and $g(\varepsilon_p)$ is a function of the pulse shaper engineering axial strain. From Eqs (12), (15), and (16)

$$\sigma_i(t) = \sigma_{st}(t) = \frac{\sigma_0 a_0}{A}\frac{g(\varepsilon_p)}{(1 - \varepsilon_p)}.\tag{17a}$$

Since the incident and striker bars remain elastic, the axial strains in the bars at the bar/pulse shaper interfaces can be written as

$$\varepsilon_i(t) = \varepsilon_{st}(t) = \frac{\sigma_0 a_0}{EA}\frac{g(\varepsilon_p)}{(1 - \varepsilon_p)}.\tag{17b}$$

The engineering strain rate in the pulse shaper is given by

$$\dot{\varepsilon}_p(t) = \frac{v_3(t) - v_4(t)}{h_0},\tag{18}$$

where $v_3(t)$ and $v_4(t)$, shown in Fig. 2(b), are the particle velocities at the striker bar/pulse shaper and incident bar/ pulse shaper interfaces. From the equations that relate stress and particle velocity in the bars, $v_3(t)$ and $v_4(t)$ are given by

$$v_3(t) = V_0 - v_{st}(t) = V_0 - \frac{\sigma_i(t)}{\rho_{st}c_{st}}\tag{19a}$$

$$v_4(t) = v_i(t) = \frac{\sigma_i(t)}{\rho c},\tag{19b}$$

where $v_{st}(t)$ and $v_i(t)$ are the particle velocities in the striker and incident bars. As shown in Figs. 1 and 2, the bar areas are equal. However, the striker bar is supported by a nylon sabot that fits into the gun barrel and this sabot mass must be included in the wave analysis for the striker bar.[24]

From Eqs (14), (18), and (19)

$$\frac{h_0}{V_0}\dot{\varepsilon}_p(t) = 1 - K\left(\frac{1}{\rho c} + \frac{1}{\rho_{st}c_{st}}\right)\frac{g(\varepsilon_p)}{1 - \varepsilon_p}, \text{ for } 0 \le t < \tau,$$
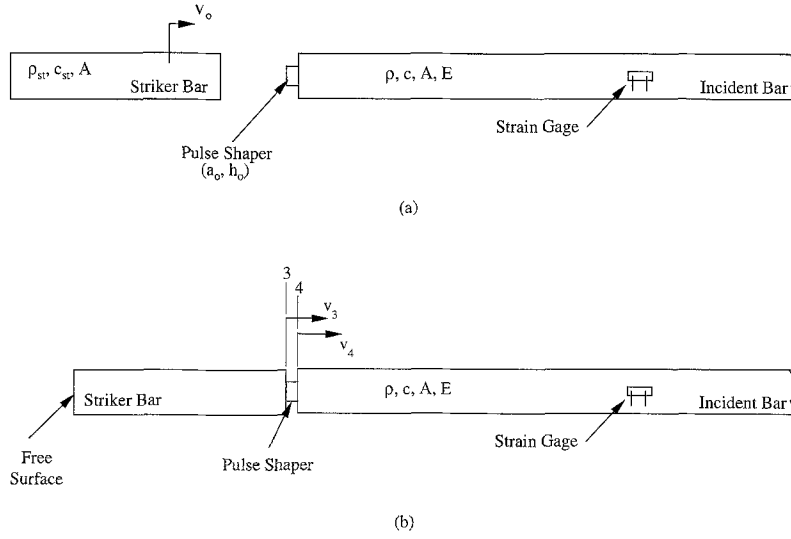
$$\tag{20}$$

**Fig. 2—Schematic of the loading end of a SHPB with a pulse shaper**

which has a solution

$$t = \frac{h_0}{V_0} \int_0^{\varepsilon_p} \left[1 - K\left(\frac{1}{\rho c} + \frac{1}{\rho_{st} c_{st}}\right) \frac{g(x)}{(1-x)}\right]^{-1} dx,$$

$$\text{for } 0 \le t < \tau \tag{21a}$$

$$K = \frac{\sigma_0 a_0}{A V_0}, \quad \text{and} \quad \tau = \frac{2L}{c_{st}}, \tag{21b}$$

where $\tau$ is equal to two wave transit times in the striker bar. Once $\varepsilon_p(t)$ is calculated from Eq (21a), the strain in the incident bar can be obtained from Eq (17b). In addition, Eq (21a) is valid only as long as the pulse shaper does not expand beyond the bar surfaces. Equation (13) shows that the engineering strain in the pulse shaper is limited for a given initial pulse shaper area $a_0$, such that $a(t) \le A$.

Equation (21a) does not explicitly give values for strain in the pulse shaper as a function of time for $0 \le t < \tau$. However, we can obtain closed-form equations for some of the features of the $\varepsilon_p$ versus $t$ curve. For small enough values of $\varepsilon_p$, the second term in Eq (20) can be neglected and

$$\varepsilon_p \approx \frac{V_0 t}{h_0} \text{ for } t << 1. \tag{22a}$$

Also, the integral in Eq (21a) must remain positive because time is always positive. Thus, the largest value of strain in the pulse shaper $\varepsilon_{pm}$ is given by

$$\frac{g(\varepsilon_{pm})}{(1 - \varepsilon_{pm})} = \frac{1}{K\left(\frac{1}{\rho c} + \frac{1}{\rho_{st} c_{st}}\right)}. \tag{22b}$$

From Eqs (17a) and (22b) the maximum possible stress in the incident bar is given by

$$\sigma_{im} = \frac{V_0}{\left(\frac{1}{\rho c} + \frac{1}{\rho_{st} c_{st}}\right)}. \tag{22c}$$

Equation (22c) gives the value of incident stress for the problem without a pulse shaper. So if the striker bar is long enough, the stress in the incident bar will approach but not exceed $\sigma_{im}$ given by (22c).

We now examine the pulse shaper response for $\tau \le t < 2\tau$. At $t = \tau/2$, the compressive wave travelling to the left in the striker bar shown in Fig. 2(b) reaches the free surface and reflects as a tensile pulse travelling to the right. At $t = \tau$, this right travelling tensile pulse reaches the striker bar/pulse shaper interface and causes additional reflected and transmitted waves to propagate in the striker and incident bars. We define $-\sigma_{st}(t - \tau)$ as the interface stress from the right travelling tensile pulse. The additional reflected and transmitted interface stresses are defined as $\sigma_r^1(t - \tau)$ and $\sigma_t^1(t - \tau)$, respectively. Thus, the axial force in the pulse shaper is given by

$$T(t) = \sigma_p(t)a(t) = [\sigma_i(t) + \sigma_t^1(t - \tau)]A$$
$$= [\sigma_{st}(t) - \sigma_{st}(t - \tau) + \sigma_r^1(t - \tau)]A. \tag{23}$$

Particle velocities at the pulse shaper/bar interfaces shown in Fig. 2(b) are

$$v_3(t) = V_0 - v_{st}(t) - v_{st}(t - \tau) - v_r^1(t - \tau)$$
$$= V_0 - \frac{\sigma_{st}(t)}{\rho_{st} c_{st}} - \frac{\sigma_{st}(t - \tau)}{\rho_{st} c_{st}} - \frac{\sigma_r^1(t - \tau)}{\rho_{st} c_{st}} \tag{24a}$$

$$v_4(t) = v_i(t) + v_t^1(t - \tau) = \frac{\sigma_i(t)}{\rho c} + \frac{\sigma_t^1(t - \tau)}{\rho c}. \tag{24b}$$

From Eqs (18), (23), and (24), the engineering strain rate is

$$h_0 \dot{\varepsilon}_p(t) = V_0 - \frac{\sigma_{st}(t)}{\rho_{st} c_{st}} - \frac{\sigma_{st}(t - \tau)}{\rho_{st} c_{st}} - \frac{\sigma_r^1(t - \tau)}{\rho_{st} c_{st}}$$
$$- \frac{\sigma_i(t)}{\rho c} - \frac{\sigma_t^1(t - \tau)}{\rho c}. \tag{25}$$

Now, we solve for $\sigma_r^1(t - \tau)$ from Eq (23) and eliminate $\sigma_r^1(t - \tau)$ from Eq (25). Thus,

$$h_0 \dot{\varepsilon}_p(t) = V_0 - \left[ \frac{1}{\rho c} + \frac{1}{\rho_{st} c_{st}} \right] \left[ \sigma_i(t) + \sigma_t^1(t - \tau) \right]$$
$$- \frac{2\sigma_{st}(t - \tau)}{\rho_{st} c_{st}}. \tag{26}$$

From Eqs (23), (16), and (13), the stress in the incident bar is

$$\sigma_i(t) + \sigma_t^1(t - \tau) = \frac{\sigma_p(t) a(t)}{A} = \frac{\sigma_0 g(\varepsilon_p) a_0}{(1 - \varepsilon_p) A}, \tag{27}$$

and from Eq (17a)

$$\sigma_{st}(t - \tau) = \frac{\sigma_0 g(\varepsilon_p(t - \tau))}{(1 - \varepsilon_p(t - \tau))} \frac{a_0}{A}. \tag{28}$$

Finally, we substitute Eqs (27) and (28) into Eq (26) and obtain

$$\frac{h_0}{V_0} \dot{\varepsilon}_p(t) = 1 - K \left( \frac{1}{\rho c} + \frac{1}{\rho_{st} c_{st}} \right) \frac{g(\varepsilon_p)}{1 - \varepsilon_p}$$
$$- \frac{2K}{\rho_{st} c_{st}} \frac{g(\varepsilon_p(t - \tau))}{1 - \varepsilon_p(t - \tau)}, \quad \text{for } \tau \le t < 2\tau. \tag{29}$$

The solution to Eq (29) is

$$t = \tau + \frac{h_0}{V_0} \int_{\varepsilon_p^1}^{\varepsilon_p} \left[ 1 - K \left( \frac{1}{\rho c} + \frac{1}{\rho_{st} c_{st}} \right) \frac{g(x)}{1 - x} \right.$$
$$\left. - \frac{2K}{\rho_{st} c_{st}} \frac{g(\varepsilon_p(t - \tau))}{1 - \varepsilon_p(t - \tau)} \right]^{-1} dx, \quad \text{for } \tau \le t < 2\tau, \tag{30}$$

where $\varepsilon_p^1$ is the strain in the pulse shaper at $t = \tau$, $\varepsilon_p(t - \tau)$ is calculated from Eq (21a) with the appropriate time shift, and $K$ and $\tau$ are defined by Eq (21b).

Equation (30) gives the total strain in the pulse shaper for $\tau \le t < 2\tau$. The strain in the incident bar is calculated from Eq (17b) using the values of $\varepsilon_p$ for $\tau \le t < 2\tau$ calculated from Eq (30). As previously mentioned, the pulse shaper must not expand beyond the bar surfaces, so the engineering strain in the pulse shaper is limited by Eq (13) for an initial pulse shaper area $a_0$, such that $a(t) \le A$. In addition, Eqs (29) and (30) are valid only if the pulse shaper remains in contraction or $\varepsilon_p(t)$ remains positive in Eq (18). Thus for the particle velocities shown in Fig. 2(b), $(v_3 - v_4) \ge 0$. When $v_3 < v_4$, the pulse shaper will be modeled as elastic unloading.

As long as $a < A$ and $v_3 > v_4$, the pulse shaper continues to deform in compression. We repeated the previous analyses for multiple reverberations in the striker bar. For $t > 2\tau$, the

general versions of Eqs (26) and (29) are

$$h_0 \dot{\varepsilon}_p(t) = V_0 - \left( \frac{1}{\rho c} + \frac{1}{\rho_{st} c_{st}} \right) \left[ \sigma_i(t) + \sigma_t^1(t - \tau) \right.$$
$$+ \sigma_t^2(t - 2\tau) + \ldots \sigma_t^n(t - n\tau) \Big]$$
$$- \frac{2}{\rho_{st} c_{st}} \left[ \sigma_{st}(t - \tau) + \sigma_r^1(t - 2\tau) \right.$$
$$+ \sigma_r^2(t - 3\tau) + \ldots \sigma_r^{(n-1)}(t - n\tau) \Big],$$
$$\text{for } n\tau \le t < (n + 1)\tau \tag{31}$$

and

$$\frac{h_0}{V_0} \dot{\varepsilon}_p(t) = 1 - K \left( \frac{1}{\rho c} + \frac{1}{\rho_{st} c_{st}} \right) \frac{g(\varepsilon_p)}{1 - \varepsilon_p}$$
$$- \frac{2K}{\rho_{st} c_{st}} \left[ \frac{g(\varepsilon_p(t - \tau))}{1 - \varepsilon_p(t - \tau)} + \frac{g(\varepsilon_p(t - 2\tau))}{1 - \varepsilon_p(t - 2\tau)} \right.$$
$$\left. + \ldots \frac{g(\varepsilon_p(t - n\tau))}{1 - \varepsilon_p(t - n\tau)} \right],$$
$$\text{for } n\tau \le t < (n + 1)\tau. \tag{32}$$

Now consider the situation when $v_3 \le v_4$ and the pulse shaper unloads during $\tau \le t < 2\tau$ at $t = t^*$. We assume the pulse shaper unloads elastically and that the unloading stress is given by

$$\sigma_u(t) = \sigma_p^* - E_p(\varepsilon_p^* - \varepsilon_p), \tag{33}$$

where $\sigma_p^*$, $\varepsilon_p^*$ are the peak stress and strain at $t = t^*$ when $v_3 = v_4$, and $E_p$ is the unloading Young's modulus.

Equation (26) gives the strain rate of the pulse shaper in terms of stress components in the incident and transmission bars for $\tau \le t < 2\tau$. For $\tau \le t < t^*$, the stress in the incident bar at the pulse shaper/incident bar interface is given by Eq (27). However, for $t^* \le t < 2\tau$, the pulse shaper is unloading. From a force balance at the pulse shaper/incident bar interface, the stress in the incident bar is

$$\sigma_i(t) + \sigma_t^1(t - \tau) = \frac{a_0 \sigma_u(t)}{A(1 - \varepsilon_p)}, \quad \text{for } t^* \le t < 2\tau. \tag{34}$$

Equation (34) assumes that the stress–strain law for the pulse shaper is given by Eq (33) and that $\sigma_u(t) \le \sigma_p^*$. The last term in Eq (26) is the interface stress from the right travelling tensile pulse coming from the free surface of the striker bar. Since this stress component is delayed by $t = \tau$, $\sigma_{st}(t - \tau)$ is given by Eq (28). We substitute Eqs (28) and (34) into Eq (26) and obtain

$$\frac{h_0}{V_0} \dot{\varepsilon}_p(t) = 1 - K \left( \frac{1}{\rho c} + \frac{1}{\rho_{st} c_{st}} \right) \frac{\sigma_p^* - E_p(\varepsilon_p^* - \varepsilon_p)}{\sigma_0(1 - \varepsilon_p)}$$
$$- \frac{2K}{\rho_{st} c_{st}} \frac{g(\varepsilon_p(t - \tau))}{1 - \varepsilon_p(t - \tau)}, \quad \text{for } t^* \le t < 2\tau, \tag{35}$$

which has solution

$$t = t^* + \frac{h_0}{V_0} \int_{\varepsilon_p^*}^{\varepsilon_p} \left[ 1 - K \left( \frac{1}{\rho c} + \frac{1}{\rho_{st} c_{st}} \right) \frac{\sigma_p^* - E_p(\varepsilon_p^* - x)}{\sigma_0(1 - x)} \right.$$

$$\left. - \frac{2K}{\rho_{st} c_{st}} \frac{g(\varepsilon_p(t - \tau))}{1 - \varepsilon_p(t - \tau)} \right]^{-1} dx, \quad \text{for } t^* \le t < 2\tau,$$

(36)

where $t^*$ is the time when $v_3 = v_4$ and unloading begins.

For many cases, additional wave reverberations in the striker bar are required to completely unload the pulse shaper. We repeated the previous analysis and obtained equations for the pulse shaper response for the onset of unloading between $\tau \le t < 2\tau$ and responses during $2\tau \le t < 3\tau$. Thus,

$$\frac{h_0}{V_0} \dot\varepsilon_p(t) = 1 - K \left( \frac{1}{\rho c} + \frac{1}{\rho_{st} c_{st}} \right) \frac{\sigma_p^* - E_p(\varepsilon_p^* - \varepsilon_p)}{\sigma_0(1 - \varepsilon_p)}$$

$$- \frac{2K}{\rho_{st} c_{st}} \frac{g(\varepsilon_p(t - \tau))}{1 - \varepsilon_p(t - \tau)} - \frac{2K}{\rho_{st} c_{st}} \frac{g(\varepsilon_p(t - 2\tau))}{1 - \varepsilon_p(t - 2\tau)},$$

$$\text{for } 2\tau \le t < \tau + t^* \quad (37a)$$

$$\frac{h_0}{V_0} \dot\varepsilon_p(t) = 1 - K \left( \frac{1}{\rho c} + \frac{1}{\rho_{st} c_{st}} \right) \frac{\sigma_p^* - E_p(\varepsilon_p^* - \varepsilon_p)}{\sigma_0(1 - \varepsilon_p)}$$

$$- \frac{2K}{\rho_{st} c_{st}} \frac{\sigma_p^* - E_p(\varepsilon_p^* - \varepsilon_p(t - \tau))}{\sigma_0(1 - \varepsilon_p(t - \tau))}$$

$$- \frac{2K}{\rho_{st} c_{st}} \frac{g(\varepsilon_p(t - 2\tau))}{1 - \varepsilon_p(t - 2\tau)}, \text{for } \tau + t^* \le t < 3\tau.$$

(37b)

Two response equations for $2\tau \le t < 3\tau$ are required because of time delay terms in Eq (31) that correspond to reverberations in the striker bar. In particular, the third terms in Eqs (37a) and (37b) are different and the other terms are the same. For $t < t^*$ the pulse shaper is loading and Eq (16) applies. By contrast, for $t \ge t^*$ the pulse shaper is unloading and Eq (33) applies.

For the situation where the pulse shaper is not fully unloaded at $t = 3\tau$, we again repeated the previous analysis and obtained equations for the pulse shaper response for unloading between $\tau \le t < 2\tau$ and responses during $3\tau \le t < 4\tau$. Thus,

$$\frac{h_0}{V_0} \dot\varepsilon_p(t) = 1 - K \left( \frac{1}{\rho c} + \frac{1}{\rho_{st} c_{st}} \right) \frac{\sigma_p^* - E_p(\varepsilon_p^* - \varepsilon_p)}{\sigma_0(1 - \varepsilon_p)}$$

$$- \frac{2K}{\rho_{st} c_{st}} \left( \frac{\sigma_p^* - E_p(\varepsilon_p^* - \varepsilon_p(t - \tau))}{\sigma_0(1 - \varepsilon_p(t - \tau))} \right.$$

$$\left. + \frac{g(\varepsilon_p(t - 2\tau))}{1 - \varepsilon_p(t - 2\tau)} + \frac{g(\varepsilon_p(t - 3\tau))}{1 - \varepsilon_p(t - 3\tau)} \right),$$

$$\text{for } 3\tau \le t < 2\tau + t^* \quad (38a)$$

$$\frac{h_0}{V_0} \dot\varepsilon_p(t) = 1 - K \left( \frac{1}{\rho c} + \frac{1}{\rho_{st} c_{st}} \right) \frac{\sigma_p^* - E_p(\varepsilon_p^* - \varepsilon_p)}{\sigma_0(1 - \varepsilon_p)}$$

$$- \frac{2K}{\rho_{st} c_{st}} \left( \frac{\sigma_p^* - E_p(\varepsilon_p^* - \varepsilon_p(t - \tau))}{\sigma_0(1 - \varepsilon_p(t - \tau))} \right.$$

$$+ \frac{\sigma_p^* - E_p(\varepsilon_p^* - \varepsilon_p(t - 2\tau))}{\sigma_0(1 - \varepsilon_p(t - 2\tau))}$$

$$\left. + \frac{g(\varepsilon_p(t - 3\tau))}{1 - \varepsilon_p(t - 3\tau)} \right),$$

$$\text{for } 2\tau + t^* \le t < 4\tau. \quad (38b)$$

Numerical evaluations helped us understand the elastic unloading process that starts when $v_3 = v_4$ and continues for $v_4 > v_3$ (see Fig. 2(b)). We found that the terms corresponding to the striker impact dominated values of $v_3$ and $v_4$. For example, the dominant term in Eq (24a) for $v_3(t)$ is $v_{st}(t) = \sigma_{st}(t)/\rho_{st} c_{st}$ and the dominant term in Eq (24b) for $v_4(t)$ is $v_i(t) = \sigma_i(t)/\rho c$. As the pulse shaper stress decreases during unloading, $\sigma_{st}(t)$ and $\sigma_i(t)$ decrease rapidly which also causes $v_3$ and $v_4$ to decrease rapidly. As $\sigma_{st}(t)$ and $\sigma_i(t)$ decrease, $v_3(t)$ decreases much more slowly than $v_4(t)$. For some cases, the unloading condition $v_3(t) \le v_4(t)$ may be violated and the pulse shaper will begin elastic loading. Due to the heavy dependence of $\sigma_i(t)$ on $v_4(t)$, this reloading is short lived, occurs frequently, and is a main reason why it is not uncommon for the unloading of the pulse shaper to be long ($\sim100$ μs). The unload/reload cycles in the pulse shaper eventually reduce the pulse shaper stress to zero and the striker and incident bars separate from each another.

In summary, we have presented a pulse shaping model for loading and unloading of the pulse shaper material. The pulse shaper material is taken as incompressible and assumed to undergo homogeneous deformation. Loading is governed by a general, one-dimensional stress–strain relationship (Eq (16)) and unloading is taken as linear (Eq (33)). A general loading equation for multiple reverberations in the striker bar is developed and given by Eq (32). The unloading procedure is more complicated and only the case for unloading at $t^*$ between $\tau \le t < 2\tau$ is presented. For other cases where unloading starts at times greater than $2\tau$, we developed a Fortran computer code[25] to calculate the pulse shaper response.

## Pulse Shaper Material Response

We present results for both hard and annealed C11000[22] copper pulse shapers. The hard copper was received from the supplier and measured 45 on the Rockwell B scale (HRB 45). We heated the as-received copper for 2 hours at 800° F to obtain the annealed copper.

The original pulse shaper geometries had thicknesses ranging from 0.8 to 1.6 mm and thickness-to-diameter ratios ranging from 0.16 to 0.50. As discussed by Kolsky,[1] Davies and Hunter,[26] and Baron,[27] these geometries can create a complicated two-dimensional stress state in the pulse shapers due to inertial and frictional effects. However, we are only attempting to produce a desired strain-time pulse in the incident bar and are not attempting to obtain stress–strain data for the pulse shapers. Thus $\sigma_p = \sigma_0 g(\varepsilon_p)$ given by Eq (16) should not be construed as a constitutive material description of the pulse shaper, but as a one-dimensional resistance function.

For the hard and annealed, C11000 copper pulse shapers, we determined that a resistance function of the form

$$\sigma_p = \frac{\sigma_0 \varepsilon_p^n}{1 - \varepsilon_p^m} \qquad (39)$$

could accurately curve fit our data with $\sigma_0$, $n$, and $m$ as adjustable parameters. Figure 3 shows the hard copper (HRB 45) resistance function with $\sigma_0 = 550$ MPa, $n = 0.0875$, and $m = 4.0$. The dashed lines are split Hopkinson pressure bar data from samples with an original diameter of 9.52 mm and an original thickness of 6.4 mm. These data reached engineering strain magnitudes of 0.44 and 0.47 with strain rates of 3200 and 3500 $s^{-1}$, respectively. The data points in Fig. 3 are from pulse shaping experiments where we used an end-point method. For the data in Table 1 and Fig. 3, the engineering strain is the final strain calculated from Eq (12). From Eqs (13) and (14), the true axial stress in the pulse shaper can be expressed in terms of strain or stress in the incident bar as

$$\sigma_p = \frac{EA}{a_0}(1 - \varepsilon_p)\varepsilon_i = \frac{A}{a_0}(1 - \varepsilon_p)\sigma_i. \qquad (40)$$

The corresponding true axial stress for each data point in Fig. 3 is that value corresponding to the maximum strain or stress measured with the incident bar that is recorded in Table 1. Thus, maximum strain is obtained from a post-test thickness measurement, and maximum stress is calculated from Eq (40) with the maximum measured strain or stress in the incident bar. Figure 3 shows that the end-point data and Hopkinson bar data are in good agreement to strains of about 0.45. The end-point method was required to obtain strain data to about 0.85.

We also present predictions from our models in Table 1. Once we obtain the parameters for the resistance function given by Eq (39), we can calculate final pulse shaper strain from Eqs (21a), (30), or (32). Peak pulse shaper stress is given by Eq (39) with the final calculated value of final pulse shaper strain. Once the calculated final stress and strain for the pulse shaper are known, we calculate maximum incident stress from Eq (40). For our SHPB experiments, the peak

incident stress predictions are the most important. Table 1 shows good agreement between measured and predicted peak incident stresses.

Figure 4 shows resistance functions for 0.79 and 1.29-mm-thick annealed copper pulse shapers. The resistance function for the 0.79-mm-thick pulse shapers lies above that for the 1.29-mm-thick pulse shapers and that suggests a slight rate effect for the material response. The parameters in Eq (39) for the annealed pulse shapers with original thickness $h_0 = 0.79$ mm are $\sigma_0 = 750$ MPa, $n = 0.37$, and $m = 4.25$; for $h_0 = 1.29$ mm, the parameters are $\sigma_0 = 625$ MPa, $n = 0.32$, and $m = 4.25$. In addition, we present results from five Hopkinson bar experiments. The data with permanent strains of 0.13, and 0.18 had an original diameter of 9.53 mm, an original thickness of 12.70 mm, and strain rates of 2100 and 3000 $s^{-1}$, respectively. The Hopkinson bar data with a permanent strain of 0.25 had an original diameter of 9.53 mm, an original thickness of 6.35 mm, and strain rate of 4370 $s^{-1}$; whereas, the Hopkinson bar data with permanent strains of 0.36 and 0.54, had an original diameter and thickness of 6.35 mm, and strain rates of 5800 $s^{-1}$ each. The end-point method data points for the 1.29-mm-thick pulse shapers are in close agreement with the Hopkinson bar data for strains to 0.55. Again, the end-point method was required to obtain strain data to about 0.85. Other data and model predictions for the annealed copper are given in Table 2.

### Incident Strain from Pulse Shaped Experiments

To obtain reliable dynamic, stress–strain data for brittle materials such as rocks or ceramics that have failure strains less than a few percent, the incident strain pulse should have a linear or quasi-linear rise. We have already used the pulse shaping techniques described in this work to conduct experiments with limestone samples[14] and will show another example with a machineable glass ceramic in the next section.

Figures 5 and 6 show data and model predictions for incident stresses from pulse shaped experiments with hard (HRB 45) and annealed C11000 pulse shapers, respectively.
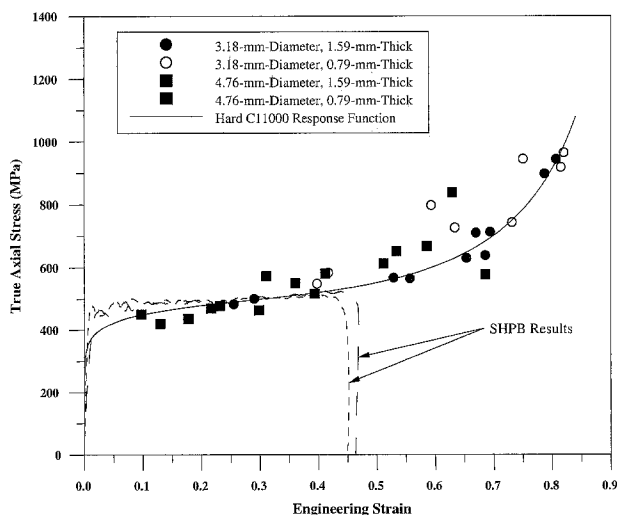


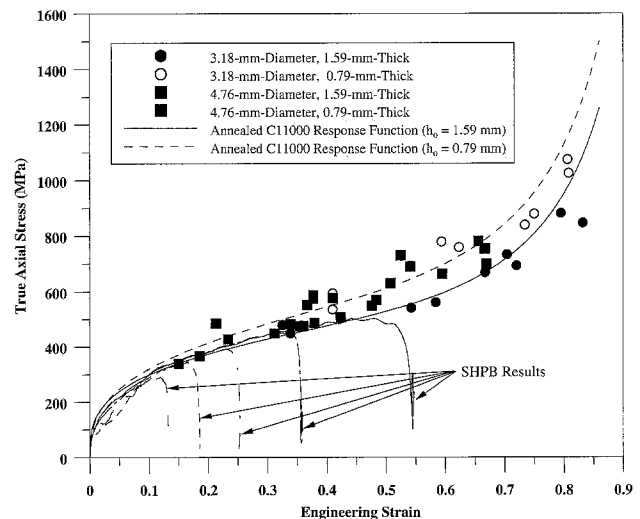Fig. 3—Data and response function for hard (HRB 45) C11000 copper



Fig. 4—Data and response functions for annealed C11000 copper

TABLE 1. POST-TEST PULSE SHAPER DATA AND MODEL PREDICTIONS FOR HARD C11000 COPPER

| Striking Velocity (m/s) | Striker Length (mm) | Initial Pulse Diameter (mm) | Initial Pulse Thickness (mm) | Final Pulse Diameter (mm) | Final Pulse Thickness (mm) | Final Pulse Axial Engineering Strain* | Peak True Pulse Shaper Stress* Stress (MPa) | Peak Incident Stress* (MPa) |
|---|---|---|---|---|---|---|---|---|
| 8.58 | 50.8 | 3.20 | 1.57 | 3.71 | 1.17 | 0.255/0.252 | 482.8/493.2 | 41.9/42.5 |
| 17.61 | 50.8 | 3.18 | 1.57 | 5.42 | 0.54 | 0.653/0.643 | 629.0/653.6 | 116.1/116.1 |
| 9.04 | 152.4 | 3.18 | 1.55 | 4.68 | 0.73 | 0.528/0.529 | 567.3/572.2 | 78.3/77.0 |
| 17.49 | 152.4 | 3.21 | 1.57 | 7.04 | 0.34 | 0.784/0.783 | 897.2/915.2 | 279.3/275.2 |
| 8.52 | 50.8 | 3.21 | 0.79 | 4.16 | 0.48 | 0.397/0.392 | 548.8/523.8 | 59.7/55.8 |
| 17.49 | 50.8 | 3.21 | 0.80 | 6.32 | 0.22 | 0.731/0.747 | 742.6/806.9 | 186.5/208.5 |
| 8.79 | 152.4 | 3.16 | 0.78 | 4.98 | 0.32 | 0.593/0.648 | 797.4/658.8 | 124.4/117.6 |
| 17.53 | 152.4 | 3.25 | 0.80 | 7.67 | 0.15 | 0.814/0.807 | 917.6/1012.4 | 339.5/349.3 |
| 8.70 | 50.8 | 4.78 | 1.59 | 5.03 | 1.44 | 0.097/0.109 | 450.3/456.5 | 71.8/73.6 |
| 17.81 | 50.8 | 4.76 | 1.59 | 6.03 | 1.02 | 0.360/0.387 | 550.0/522.5 | 126.0/121.3 |
| 8.66 | 152.4 | 4.74 | 1.58 | 5.46 | 1.21 | 0.232/0.241 | 478.0/490.9 | 89.6/91.5 |
| 17.50 | 152.4 | 4.74 | 1.59 | 7.41 | 0.66 | 0.585/0.607 | 667.2/621.4 | 230.6/223.9 |
| 8.69 | 50.8 | 4.81 | 0.77 | 5.42 | 0.64 | 0.178/0.189 | 436.2/479.7 | 80.7/86.0 |
| 17.76 | 50.8 | 4.78 | 0.78 | 6.92 | 0.38 | 0.511/0.545 | 612.1/580.9 | 184.5/183.3 |
| 8.68 | 152.4 | 4.75 | 0.78 | 5.80 | 0.54 | 0.311/0.363 | 572.7/517.1 | 121.1/115.2 |
| 17.52 | 152.4 | 4.78 | 0.81 | 7.87 | 0.30 | 0.629/0.694 | 838.0/712.5 | 326.7/335.3 |

*Experimental data/model prediction

NOTE: The bar diameters were 12.7 mm. For the 50.8 mm and 152.4 mm long striker bars $\rho_{st}$ = 10730 kg/m$^3$ and 8750 kg/m$^3$, respectively.

TABLE 2. POST-TEST PULSE SHAPER DATA AND MODEL PREDICTIONS FOR ANNEALED C11000 COPPER

| Striking Velocity (m/s) | Striker Length (mm) | Initial Pulse Diameter (mm) | Initial Pulse Thickness (mm) | Final Pulse Diameter (mm) | Final Pulse Thickness (mm) | Final Pulse Axial Engineering Strain* | Peak True Pulse Shaper Stress* (MPa) | Peak Incident Stress* (MPa) |
|---|---|---|---|---|---|---|---|---|
| 8.55 | 50.8 | 3.18 | 1.57 | 3.93 | 1.04 | 0.339/0.335 | 447.9/449.8 | 43.6/42.9 |
| 17.68 | 50.8 | 3.19 | 1.60 | 5.57 | 0.53 | 0.667/0.663 | 669.3/682.5 | 130.5/129.4 |
| 8.72 | 152.4 | 3.19 | 1.61 | 4.78 | 0.73 | 0.543/0.544 | 541.1/565.0 | 77.9/79.5 |
| 17.49 | 152.4 | 3.20 | 1.59 | 7.11 | 0.33 | 0.795/0.782 | 881.0/951.2 | 280.2/281.5 |
| 8.16 | 50.8 | 3.18 | 0.77 | 4.20 | 0.46 | 0.410/0.418 | 535.3/564.0 | 59.4/61.6 |
| 17.63 | 50.8 | 3.18 | 0.80 | 6.21 | 0.21 | 0.734/0.727 | 838.7/942.4 | 203.4/219.8 |
| 8.67 | 152.4 | 3.19 | 0.80 | 5.03 | 0.33 | 0.594/0.610 | 779.2/729.2 | 124.1/120.7 |
| 17.57 | 152.4 | 3.20 | 0.81 | 7.34 | 0.16 | 0.808/0.787 | 1024.5/1165.2 | 347.1/350.4 |
| 8.31 | 50.8 | 4.77 | 1.57 | 5.26 | 1.34 | 0.150/0.169 | 340.0/358.7 | 59.3/61.8 |
| 17.61 | 50.8 | 4.79 | 1.58 | 6.41 | 0.91 | 0.424/0.438 | 507.4/500.5 | 131.2/128.3 |
| 8.63 | 152.4 | 4.77 | 1.57 | 5.81 | 1.08 | 0.312/0.320 | 448.6/442.11 | 95.3/93.1 |
| 17.52 | 152.4 | 4.81 | 1.62 | 7.60 | 0.66 | 0.594/0.617 | 663.8/628.4 | 240.7/238.6 |
| 8.68 | 50.8 | 4.76 | 0.76 | 5.55 | 0.58 | 0.233/0.252 | 427.3/458.1 | 82.6/87.4 |
| 17.74 | 50.8 | 4.80 | 0.82 | 6.94 | 0.4 | 0.508/0.531 | 631.5/648.8 | 191.5/200.1 |
| 8.51 | 152.4 | 4.78 | 0.76 | 6.01 | 0.48 | 0.367/0.387 | 552.4/545.6 | 125.3/127.5 |
| 17.48 | 152.4 | 4.78 | 0.78 | 8.15 | 0.27 | 0.656/0.663 | 781.3/808.6 | 326.6/343.7 |

*Experimental data/model prediction

NOTE: The bar diameters were 12.7 mm. For the 50.8 mm and 152.4 mm long striker bars $\rho_{st}$ = 10730 kg/m$^3$ and 8750 kg/m$^3$, respectively.
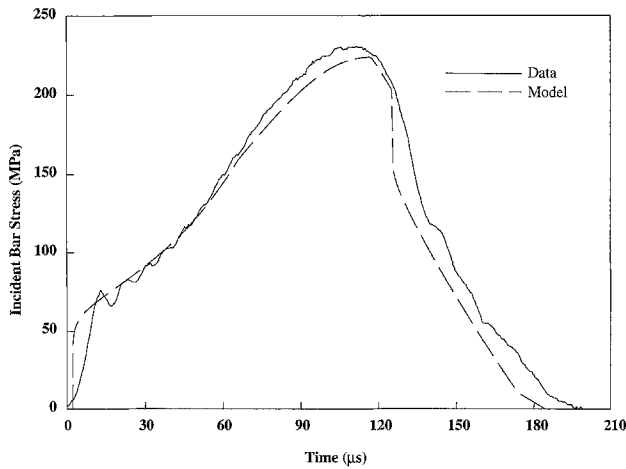
Fig. 5—Incident bar stress data and model prediction for a hard (HRB 45) C11000 copper pulse shaper
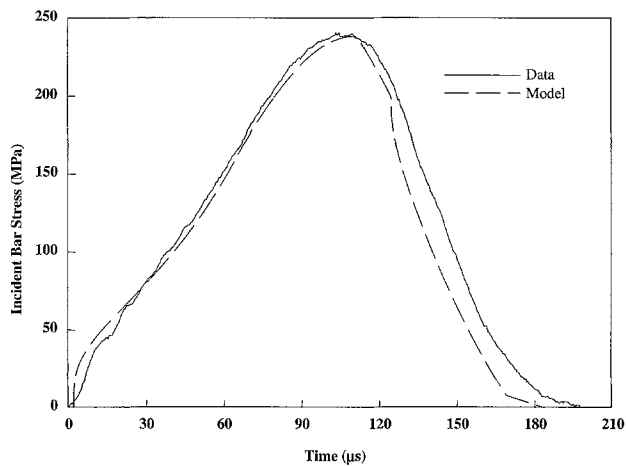


Fig. 6—Incident bar stress data and model prediction for an annealed C11000 copper pulse shaper

The pulse shapers had original thicknesses and diameters of 1.6 mm and 4.8 mm, respectively. The striker and incident bars shown in Fig. 2(a) had 12.7-mm diameters and the striker length was 152 mm.

We previously defined $\tau$ with Eq (21b) as the time for two wave transit times in a striker bar of length $L$. For the data and model predictions shown in Figs. 5 and 6, the experiments were conducted with $\rho_{st} = 8750$ kg/m$^3$, $c_{st} = 4780$ m/s, $L = 152$ mm, $\tau = 63.6$ $\mu$s, and a striking velocity $V_0 = 17.5$ m/s. Both Figs. 5 and 6 show that the onset of unloading is at about $t^* = 110$ $\mu$s. So $\tau \leq t^* < 2\tau$, and the loading strain in the pulse shaper is calculated from Eq (21a) for $0 \leq t < \tau$ and from Eq (30) for $\tau \leq t < t^*$. However, as with all Hopkinson experimental techniques, we do not measure stresses or strains in the pulse shaper but infer these quantities through a wave analysis and downstream strain measurements on the incident bar. Thus, the model that predicts incident bar stresses shown in Figs. 5 and 6 are calculated from Eqs (16), (17a), and (39).

For $t \geq t^*$ or $t$ greater than about 110 $\mu$s, the pulse shaper is unloading. We take the unloading Young's modulus as

$E_p = 117$ GPa in Eq (33) and calculate the unloading pulse shaper strain responses for $t^* \leq t < 2\tau(2\tau = 127$ $\mu$s) from Eq (36) and for $2\tau \leq t < 3\tau (3\tau = 191$ $\mu$s) from Eqs (37a) and (37b). The incident bar stresses predicted for unloading in Figs. 5 and 6 can be expressed in terms of the strain in the pulse shaper. We combine Eqs (13), (14), and (33) and obtain

$$\sigma_i = \frac{a_0}{A(1 - \varepsilon_p)}\sigma_p^* - E_p\left(\varepsilon_p^* - \varepsilon_p\right), \tag{41}$$

where $\sigma_p^*$ and $\varepsilon_p^*$ are the peak pulse shaper stress and strain at the onset of unloading.

A common feature for the hard copper data is a well-defined kink found early in the incident stress–time data. The kink shown in Fig. 5 has an incident stress level of about 70 MPa and is caused by the transition from elastic to plastic deformation in the pulse shaper. The incident stress level of this kink can be adjusted by changing the initial pulse shaper diameter. In addition, the data in Fig. 6 show the kink is removed for an annealed copper pulse shaper that has a very small yield strength.

## Modified SHPB Experiments with Macor

The analytical models presented in the section entitled *Models for Sample Equilibrium and Constant Strain Rate* examine the sample response produced by an incident stress pulse. The incident stress pulse given by Eq (7) is taken as a quadratic function, but these models assume the sample has a linear stress–strain response. While most brittle materials, such as rocks[14] or ceramics, have quasi-linear, dynamic stress–strain responses, slight deviations from linear can change the strain-rate histories over the test duration. Because we do not know the sample, stress–strain response before a test, some experimental trials are required before we achieve dynamic stress equilibrium and nearly constant strain rate. The analytical models show trends that help guide and minimize our experimental trials.

We begin this process by first conducting a few quasi-static, stress–strain experiments with a new sample material. Then, we linearize this quasi-static data and obtain a value for $E_s$ for Eq (6). Our early SHPB experiments are conducted with nearly linear incident stress pulses such as those for limestone[14] or the incident pulse shown in Fig. 6. We check for sample equilibrium and nearly constant strain rate with strain measurements and Eqs (1a), (1b), and (3). In this study, we learned that it was relatively easy to obtain sample equilibrium and more difficult to obtain a nearly constant strain rate over most of the test duration. For the Macor results presented in this section, analytical and experimental trials suggest the concave downward incident stress pulse shown in Fig. 7 produced a nearly constant strain rate.

To demonstrate our modified SHPB technique, we present results from two pulse shaped experiments with the machine-able glass ceramic, Macor.[23] Data from experiments with Macor show that the samples are in dynamic stress equilibrium and have nearly constant strain rates over most of the duration of the tests. In addition, we carefully bracket sample failure with one test where the sample fails with catastrophic damage and a second test where the sample is recovered intact. Thus, intact samples that experience strains beyond the elastic region and post-peak stresses can be retrieved for microstructural evaluations.
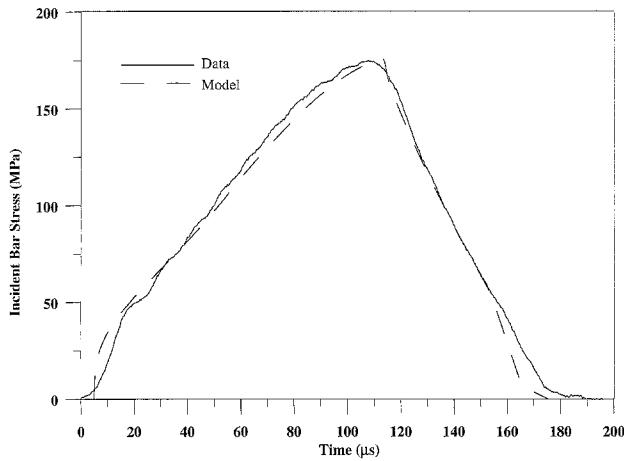
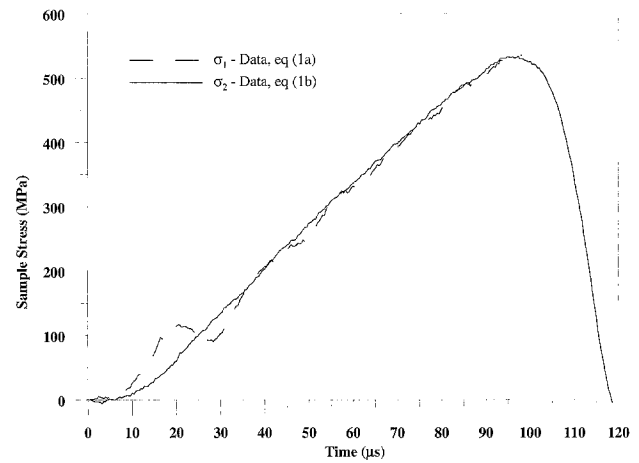Fig. 7—Incident bar stress data and model prediction for an annealed C11000 copper pulse shaper



Fig. 8—Interface stresses from a pulse shaped SHPB experiment with a Macor sample
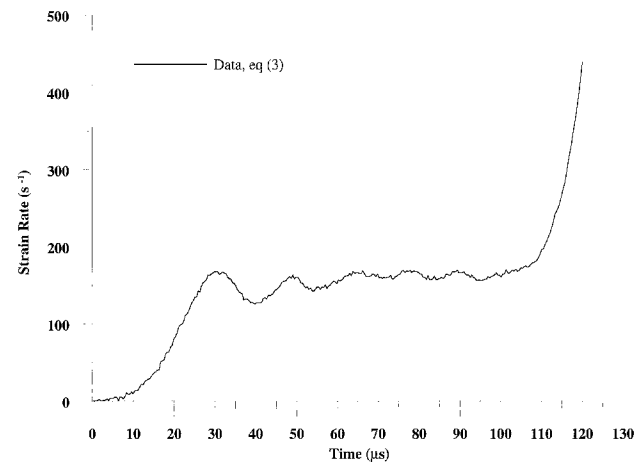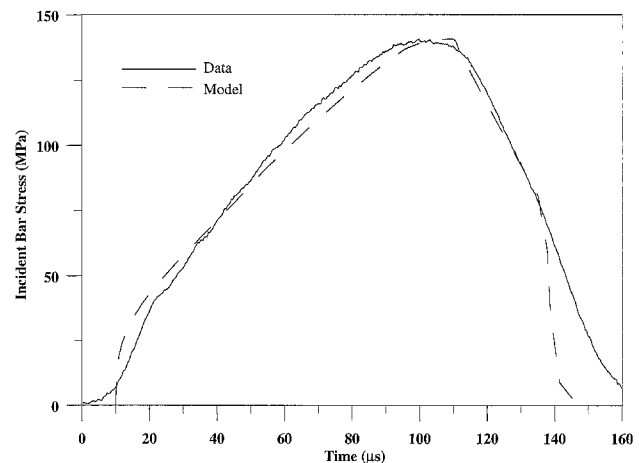


Fig. 9—Strain rate from a pulse shaped SHPB experiment with a Macor sample



Fig. 10—Incident bar stress data and model prediction for an annealed C11000 copper pulse shaper

The striker, incident, and transmission bars shown in Fig. 1 had diameters of 19.05 mm. The Macor samples had a length and diameter of 9.53 mm. To obtain incident stress pulses that would strain the Macor samples at a nearly constant strain rate over most of the test durations, 7.15-mm-diameter, 1.59-mm-thick, annealed C11000 copper pulse shapers were used. All of the above mentioned parameters remained fixed for the two experiments presented in this section. However, the first experiment used a 127.0-mm-long striker bar, and the second experiment used a 101.6-mm-long striker bar. The effective densities and wave velocities that correct for the added mass of the sabots were $\rho_{st} = 8790$ kg/m$^3$, $c_{st} = 4770$ m/s and $\rho_{st} = 8760$ kg/m$^3$, $c_{st} = 4780$ m/s for the 127.0-mm-long and 101.6-mm-long striker bars, respectively. The 127.0-mm-long striker bar was launched to a striking velocity of 15.0 m/s while the 101.6-mm-long striker bar was launched at 14.4 m/s.

Figures 7, 8, and 9 show data for the experiment conducted with the 127.0-mm-long striker bar. In Figure 7, we show the measured incident stress pulse and a prediction from our pulse shaping model. Figure 8 shows stresses at stations 1 and 2 shown in Fig. 1. The stress at the incident bar/sample interface $\sigma_1$ is calculated from Eq (1a) and strains measured on the incident bar, and stress at the transmission bar/sample interface $\sigma_2$ is calculated from Eq (1b) and the measured transmitted strain. These interface stresses are in reasonably good agreement, which implies that the sample is nearly in dynamic stress equilibrium. Strain rate in the sample, shown in Fig. 9, is calculated from Eq (3) and the measured reflected strain in the incident bar. The average strain rate is about 160 s$^{-1}$ over 25 $\mu$s to 105 $\mu$s. At about 105 $\mu$s the sample begins to fail and eventually fails with catastrophic damage.

Figures 10, 11, and 12 show data for the experiment conducted with the 101.6-mm-long striker bar. Figure 12 shows an average strain rate of 130 s$^{-1}$ over 35 $\mu$s to 85 $\mu$s. At 110 $\mu$s, the sample unloads and was recovered intact.

Figure 13 shows dynamic and quasi-static stress–strain data for the Macor samples. The sample with an average strain rate of $\varepsilon_s = 130$ s$^{-1}$ experienced strain beyond the elastic region and post-peak stress. Samples such as these can be retrieved for post-test, microstructural evaluations.
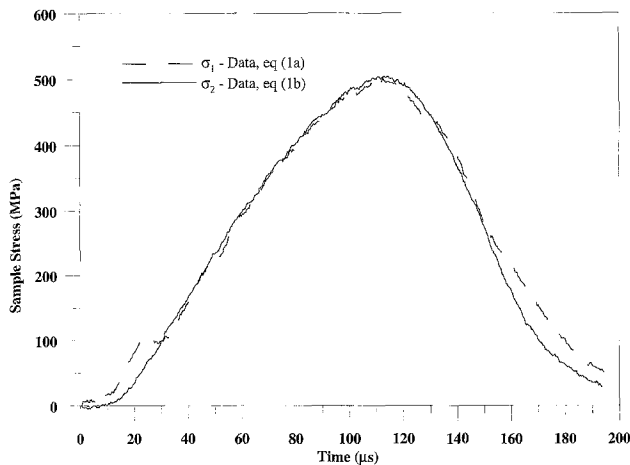
Fig. 11—Interface stresses from a pulse shaped SHPB experiment with a Macor sample
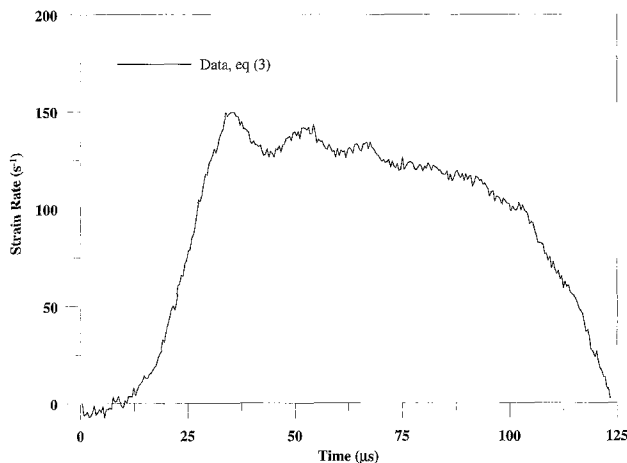


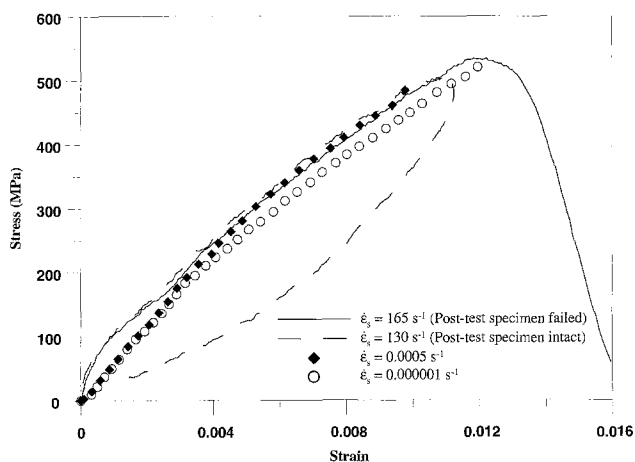Fig. 12—Strain rate from a pulse shaped SHPB experiment with a Macor sample



Fig. 13—Quasi-static and dynamic stress–strain data for Macor

## Summary

We present analytical models and experimental techniques that provide procedures to obtain dynamic, compressive stress–strain data for brittle materials. The conventional split Hopkinson pressure bar apparatus is modified by shaping the incident pulse such that the samples are in dynamic stress equilibrium and have nearly constant strain rate over most of the test duration. A thin disk of annealed or hard C11000 copper is placed on the impact surface of the incident bar in order to shape the incident pulse. After impact by the striker bar, the copper disk deforms plastically and spreads the pulse in the incident bar. We present an analytical model and data that show a wide variety of incident strain pulses can be produced by varying the geometry of the copper disks and the length and striking velocity of the striker bar. Model predictions are in good agreement with measurements. In addition, we present data for a machineable glass ceramic material, Macor, that shows pulse shaping is required to obtain dynamic stress equilibrium and nearly constant strain rate over most of the test duration.

## Acknowledgments

## References

1. Kolsky, H., "An Investigation of the Mechanical Properties of Materials at Very High Rates of Loading," Proc. Royal Soc. Lond., B, **62**, 676–700 (1949).

2. Kolsky, H., Stress Waves in Solids, Dover, New York (1963).

3. Nicholas, T., "Material Behavior at High Strain Rates," Impact Dynamics, Chap. 8, John Wiley & Sons, New York (1982).

4. Ellwood, S., Griffiths, L. J., and Parry, D. J., "Materials Testing at High Constant Strain Rates," J. Phys. E: Sci. Instrum., **15**, 280–282 (1982).

5. Franz, C. E., Follansbee, P. S., and Wright, W. J., "New Experimental Techniques with the Split Hopkinson Pressure Bar," in the 8th International Conference on High Energy Rate Fabrication, Pressure Vessel and Piping Division, ASME, I. Berman and J. W. Schroeder, eds., San Antonio, TX (1984).

6. Follansbee, P. S., "The Hopkinson Bar," Mechanical Testing, Metals Handbook, 9th ed., **8**, American Society for Metals, Metals Park, Ohio, 198–217 (1985).

7. Nemat-Nasser, S., Isaacs, J. B., and Starrett, J. E., "Hopkinson Techniques for Dynamic Recovery Experiments," Proc. R. Soc. Lond., A, **435**, 371–391 (1991).

8. Ramesh, K. T. and Narasimhan, S., "Finite Deformations and the Dynamic Measurement of Radial Strains in Compression Kolsky Bar Experiments," Int. J. Solids Structures, **33**, 3723–3738 (1996).

9. Gray, G. T., "Classic Split-Hopkinson Pressure Bar Technique," ASM Handbook, **8**, Mechanical Testing and Evaluation, ASM International, Materials Park, OH, 44073-0002 (2000).

10. Gray, G. T. and Blumenthal, W. R., "Split-Hopkinson Pressure Bar Testing of Soft Materials," ASM Handbook, **8**, Mechanical Testing and Evaluation, ASM International, Materials Park, OH, 44073-0002 (2000).

11. Yadav, S., Chichili, D. R., and Ramesh, K. T., "The Mechanical Response of a 6061-T6 Al/Al2O3 Metal Matrix Composite at High Rates of Deformation," Acta metall. Mater., **43**, 4453–4464 (1995).

12. Rogers, W. P. and Nemat-Nasser, S., "Transformation Plasticity at High Strain Rate in Magnesia-Partially-Stabilized Zirconia," J. Am. Ceram. Soc., **73**, 136–139 (1990).

13. Chen, W. and Ravichandran, G., "Dynamic Compressive Failure of a Glass Ceramic Under Lateral Confinement," J. Mech. Phys. Solids. **45**, 1303–1328 (1997).

14. Frew, D. J., Forrestal, M. J., and Chen, W., "A Split Hopkinson Bar Technique to Determine Compressive Stress–strain Data for Rock Materials," EXPERIMENTAL MECHANICS, **41**, 40–46 (2001).

15. Follansbee, P. S., and Franz, C. E., "Wave Propagation in the Split Hopkinson Pressure Bar," Trans. ASME, J. Eng. Mat. Technol., **105**, 61–66 (1983).

16. Duffy, J., Campbell, J. D., and Hawley, R. H., "On the Use of a Torsional Split Hopkinson Bar to Study Rate Effects in 1100-0 Aluminum," ASME J. Appl. Mech., **37**, 83–91 (1971).

17. Wu, X. J. and Gorham, D. A., "Stress Equilibrium in the Split Hopkinson Pressure Bar Test," J. PHYS. IV FRANCE, **7**, C3, 91–96 (1997).

18. Togami, T. C., Baker, W. E. and Forrestal, M. J., "A Split Hopkinson Bar Technique to Evaluate the Performance of Accelerometers," J. Appl. Mech., **63**, 353–356 (1996).

19. Chen, W., Zhang, B., and Forrestal, M. J., "A Split Hopkinson Bar Technique for Low-Impedance Materials," EXPERIMENTAL MECHANICS, **39**, 81–85 (1999).

20. Christensen, R. J., Swanson, S. R., and Brown, W. S., "Split-Hopkinson-Bar Tests on Rock Under Confining Pressure," EXPERIMENTAL MECHANICS, **29**, 508–513 (1972).

21. Ravichandran, G. and Subhash, G., "Critical Appraisal of Limiting Strain Rates for Compression Testing of Ceramics in a Split Hopkinson Pressure Bar," J. Am. Ceram. Soc., **77**, 263–267 (1994).

22. Lewis, C. F., "Properties and Selection: Nonferrrous Alloys and Pure Metals," In Metals Handbook, 9th Edition, **2**, American Society for Metals, Metals Park, OH (1979).

23. Corning Incorporated, "Macor Machineable Glass Ceramic: Safety and Health Issues," Technical Bulletin, Macor-03, Corning, New York (1992).

24. Forrestal, M. J., Frew, D. J., and Chen, W., "The Effect of Sabot Mass on the Striker Bar for Split Hopkinson Pressure Bar Experiments," Unpublished Manuscript.

25. Frew, D. J., "The Dynamic Response of Brittle Materials from Penetration and Split Hopkinson Pressure Bar Experiments," Ph.D. thesis, Arizona State University (2000).

26. Davies, E. D. H. and Hunter S. C. "The Dynamic Compression Testing of Solids by the Method of the Split Hopkinson Pressure Bar," J. Mech. Phys. Solids, **11**, 155–179 (1963).

27. Baron, H. G. "Stress/Strain Curves for Some Metals and Alloys at Low Temperatures and High Rates of Strain," J. Iron St. Inst., **182**, 354–365 (1956).